Investigating the role of stratospheric ozone as a driver of inter-model spread in CO_2 effective radiative forcing.

Rachael E. Byrom[1], Gunnar Myhre[1], Øivind Hodnebrog[1], Dirk Olivié[2], Michael Schulz[2]

[1]CICERO, Oslo, 0318, Norway
[2]Norwegian Meteorological Institute, Oslo, 0313, Norway

Correspondence to: Rachael E. Byrom (rachael.byrom@cicero.oslo.no)

Abstract. Addressing the cause of inter-model spread in carbon dioxide (CO_2) radiative forcing is essential for reducing uncertainty in estimates of climate sensitivity. Recent studies demonstrate that a large proportion of this spread arises from variance in model base-state climatology, particularly the specification of stratospheric temperature, which itself plays a dominant role in determining the magnitude of CO_2 forcing. Here we investigate stratospheric ozone (O_3) as a cause of inter-model differences in stratospheric temperature, and hence its role as a contributing factor to spread in CO_2 radiative forcing. We use the Norwegian Earth System Model 2 (NorESM2) to analyse the impact of systematic increases/decreases in stratospheric O_3 on the magnitude of 4xCO_2 effective radiative forcing (ERF) and its components. Firstly, we demonstrate that accurate estimation of instantaneous radiative forcing (IRF) requires the use of host-model radiative transfer calculations. Secondly, we show that a 50% increase and decrease in stratospheric O_3 concentration leads to significant differences in base-state stratospheric temperature, ranging from +6 K to -9 K, respectively. These experiments impact the IRF due to the influence of base-state stratospheric temperature on the emission of outgoing longwave radiation and the spectral overlap of CO_2 and O_3. However, the impact on IRF does not result in a correspondingly large spread in CO_2 ERF. We conclude that inter-model differences in stratospheric O_3 concentration are therefore not predominantly responsible for inter-model spread in CO_2 ERF.

1 Introduction

Effective radiative forcing (ERF) quantifies the top-of-atmosphere (TOA) perturbation to the Earth's energy balance imposed by a forcing mechanism, such as CO_2, aerosols or solar irradiance. It includes the instantaneous radiative forcing (IRF; i.e., the initial radiative response to the perturbation) and the subsequent radiative effect of adjustments in tropospheric and stratospheric temperature, water vapour, surface albedo and clouds, which each cause an impact on TOA radiative fluxes (Myhre et al., 2013; Boucher et al., 2013; Sherwood et al., 2015; Forster et al., 2021).

ERF can be expressed simply (following e.g., Chung and Soden 2015a; Smith et al., 2018) as:

$$ERF = IRF + A_{T_{Strat}} + A_{T_{Trop}} + A_{H_2O} + A_\alpha + A_c + \epsilon, \quad (1)$$

whereby ERF is the net (shortwave plus longwave) change in downward TOA flux (W m^{-2}), IRF is the direct net change in downward TOA flux (W m^{-2}), A_x is the radiative adjustment from stratospheric temperature (T_{strat}), tropospheric temperature (T_{Trop}), water vapour (H_2O), surface albedo (α) and clouds (c), with ϵ representing a non-linear residual term that is typically small (around 10% of the ERF; Shell et al., 2008).

ERF is used extensively to compare the relative strength of different forcing agents. Historically, quantifying the climate impact of a given agent commonly relied solely on diagnosing its IRF or stratospheric temperature adjusted radiative forcing (SARF, e.g., Ramaswamy et al., 2019). However, given that additional so-called 'adjustments' develop from the initial radiative perturbation and impact the TOA imbalance, it is also necessary to include them in the radiative forcing framework. Consequently, this has been shown to improve the utility of the radiative forcing metric in predicting global-mean surface temperature change (ΔT_s), ultimately due to a more realistic separation of forcing from surface-temperature driven feedbacks (e.g. Sherwood et al., 2015; Marvel et al., 2016; Richardson et al., 2019). Adjustments therefore form an important component of climate change assessment and necessitate the use of climate model integrations to simulate the radiative response of tropospheric and land surface changes to TOA energy imbalance, in addition to the traditional diagnostic of IRF or SARF, which can be calculated using offline radiative transfer codes or simplified expressions (e.g. Hansen et al., 1988; Myhre et al., 1998; Etminan et al., 2016; Meinshausen et al., 2020). This makes ERF considerably more computationally-expensive to estimate and introduces more model diversity driven uncertainty. The use of different methods to calculate ERF further complicates inter-model comparison, with some studies opting to diagnose the forcing from fixed sea-surface temperature (SST) and sea ice simulations (Hansen et al., 2005), or alternatively, by regressing TOA irradiance against global surface temperature change (Gregory et al., 2004; see Forster et al., 2016).

For CO_2, inter-model spread in ERF remains an ongoing issue. Smith et al. (2020a) report a 4xCO_2 ERF range of 7.3-8.9 W m^{-2} for 17 CMIP6 (Coupled Model Intercomparison Project Phase 6; Eyring et al., 2016) models contributing to the Radiative Forcing Model Intercomparison Project (RFMIP; Pincus et al., 2016), which aims to achieve accurate characterisation of ERF through consistent diagnosis with the fixed-SST method (Forster et al., 2016). Whilst this spread has been reduced compared to earlier analysis of 13 CMIP5 models (Kamae and Watanabe 2012; see Smith et al., 2020a Fig. 5), identifying and remedying the exact nature of CO_2 ERF diversity is an active area of research (e.g., Soden et al., 2018; Pincus et al., 2016; Smith et al., 2020a). Several studies show that model differences in the magnitude of IRF contributes significantly (e.g., Zhang and Huang 2014; Chung and Soden 2015b; Andrews et al., 2015), arising either from radiative transfer parameterisation error (e.g., Collins et al., 2006; Pincus et al., 2015) and/or differences in model base-state climatology (Pincus et al., 2020; Jeevanjee et al., 2021). Recently, He et al., (2023) more specifically attribute this base-state dependence to stratospheric temperature. They report a significant correlation between 4xCO_2 IRF and 10 hPa air temperature in CMIP5/6 models, demonstrating that biases in stratospheric temperature play a leading role in causing inter-model CO_2 IRF spread. Given that IRF accounts for around 60%

of CO_2 ERF and that stratospheric cooling is its dominant adjustment (Myhre et al., 2013; Smith et al., 2018), examining potential causes of model differences in stratospheric temperature presents a clear opportunity to further current understanding.

One such cause could relate to stratospheric O_3 – a key constituent in modulating stratospheric temperature. Depending on the treatment of stratospheric chemistry, models adopt a range of methods to generate O_3 fields using either an interactive chemistry scheme, a simplified online scheme or a prescribed pre-simulated dataset. Consequently, the resulting spatial structure and regional distribution of concentrations can differ substantially. Keeble et al. (2021) evaluate long-term O_3 trends in 22 CMIP6 models and find poor agreement in the simulation of pre-industrial total column ozone (TCO), with a variation from 275 to 340 DU between 60˚N-60˚S. Further, a ~ 20 DU range is observed between 10 of the models that prescribe stratospheric O_3 according to the CMIP6 O_3 dataset (Checa-Garcia, 2018), highlighting that even the model-specific implementation of common input can lead to significant differences in TCO.

Here, we perform idealised experiments (Section 2) to investigate the role of stratospheric O_3 as a driver of inter-model diversity in stratospheric temperature, and hence its role as a driver of spread in CO_2 ERF. First, we examine 4xCO_2 ERF and compare our results to previous estimates, with a particular focus on the diagnosis of IRF and T_{strat} (Section 3). We then investigate the impact of stratospheric O_3 specification on each component of 4xCO_2 ERF (Section 4).

2 Models, experiments and methods

We use atmosphere-only simulations from NorESM2-MM (Seland et al., 2020) to calculate ERF following an abrupt quadrupling of CO_2 relative to pre-industrial (1850) conditions (see Text S1 in the Supplement for further detail on model configuration). This model is used to perform a baseline (control) integration and a perturbed (4xCO_2) integration using prescribed SST and sea-ice extent climatologies; hence we use the fixed-SST method to diagnose forcing as recommended by RFMIP (Pincus et al., 2016) whereby ERF is calculated as the difference in TOA net radiative flux between the perturbed and control simulations. Integrations are run for 30 years, with years 6 to 30 used for analysis in Section 3. This simulation length was chosen to allow for better comparison of our results against the 30-year NorESM2-MM 4xCO_2 ERF experiments of Smith et al. (2020a).

We perform two further 4xCO_2 ERF experiments whereby stratospheric O_3 is increased by 50% (Strat O_3x1.5) and decreased by 50% (Strat O_3x0.5) relative to its pre-industrial concentration. Considering the substantial range in pre-industrial TCO noted by Keeble et al. (2021, Figure A3), we choose such a large, idealised increase/decrease in attempt to cover a broader range of stratospheric O_3 than shown by CMIP6 models, thus any effect on 4xCO_2 ERF would likely be amplified in comparison.

Note that in each ERF experiment the O_3 increase (or decrease) is applied to both the control and $4xCO_2$ simulation so that the new O_3 field acts exclusively to alter the base-state atmosphere and does not act as a forcing itself. As in the 'standard' $4xCO_2$ ERF experiment described above, stratospheric O_3 fields are prescribed using output from the Community Earth System Model version 2 - Whole Atmosphere Community Climate Model version 6 (CESM2-WACCM6; Gettelman et al., 2019) as zonally-averaged 5 day fields (Fig. S1). A linearly varying tropopause (from 100hPa at the equator to 300 hPa at the poles) is used to delineate the stratosphere and troposphere (Soden et al., 2008, Smith et al. 2018). O_3 concentrations above this boundary are multiplied by 1.5 and 0.5 to increase and decrease levels by 50%, respectively. These simulations are run for 15 years to reduce computational expense, with years 6 to 15 of each integration used for analysis (Section 4). Table S1 summarises all experiments.

IRF is calculated using the Parallel Offline Radiative Transfer (PORT; Conley et al., 2013) code. This code isolates the radiative transfer scheme employed by NorESM2-MM (i.e., RRTMG, Iacono et al., 2008) to provide stand-alone offline radiation diagnostics. It is used here to perform two sets of radiative transfer calculations for each experiment listed in Table S1; a baseline (control) simulation and a perturbed ($4xCO_2$) simulation, which are both run using 12-month climatology from the corresponding ERF control integration (i.e., the first 12 months of its output). Simulations are then run for 12 months to diagnose annual-mean IRF as the difference in TOA net radiative flux between the perturbed and control run.

Corresponding radiative adjustments are quantified using radiative kernels (Soden et al., 2008). Summarising the more detailed description given by Smith et al. (2018), these characterise the change in TOA radiative flux ΔR (either shortwave or longwave) following a unit change in a state variable (Δx), e.g., temperature, surface albedo or water vapour. They are constructed by running a climate model's offline radiative transfer code twice, once with a baseline climatology and again with a unit change in x to calculate ΔR. The radiative kernel (K_x) is given by:

$$K_x = \frac{\partial R}{\partial x}. \tag{2}$$

The corresponding adjustment (A_x) is then quantified as:

$$A_x = K_x(x_p - x_c), \tag{3}$$

whereby $x_p - x_c$ represents the difference in x between the perturbed and control atmosphere-only climate model integrations, respectively. Here, A_x is calculated using output from NorESM2-MM with radiative kernels derived from three models: the Community Earth System Model 1-Community Atmosphere Model 5 (CESM-CAM5, Pendergrass et al., 2018), the Hadley Centre Global Environment Model 3-GA7.1 (HadGEM3-GA7.1, Smith et al., 2020b), and the European Centre for

Medium-Range Weather Forecasts (ECMWF)-Oslo model (Myhre et al., 2018). We use kernels to calculate all adjustments given in Eq. (1) except for A_c which cannot be directly calculated from a kernel since the radiative effects of clouds are too nonlinear (Soden et al., 2008). To estimate A_c we calculate the difference between clear-sky and all-sky TOA ERF (i.e., the cloud radiative effect; CRE) and then modify this to correct for cloud masking of the clear-sky 4xCO_2 forcing and adjustment response (see Soden et al., 2008) This differs from alternate approaches used to calculate A_c such as the kernel-difference method, which involves differencing all-sky and clear-sky ERF, IRF and the sum of adjustments (e.g., Soden et al., 2008; Smith et al., 2018; Smith et al., 2020a), and the approximate partial radiative perturbation (APRP) method, which estimates shortwave cloud responses from climate model diagnostics (Zelinka et al., 2014; Smith et al., 2018). Additionally, we also use kernels to calculate the adjustment due to surface temperature change (A_{T_S}) as in Smith et al. (2018), since land surface temperatures are allowed to respond to the forcing in our simulations given the difficulty in prescribing fixed surface temperatures (Forster et al., 2016). Several studies also follow this approach whereby the calculation of ERF includes the radiative response of land surface warming or cooling (e.g., Hansen et al., 2005; Forster et al., 2016; Smith et al., 2018; Smith et al., 2020a). Generally, methods that correct for this produce a slightly larger ERF following a CO_2 perturbation (Smith et al., 2020a; Andrews et al., 2021). Further, we use the same tropopause definition as above to delineate $A_{T_{Strat}}$ and $A_{T_{Trop}}$.

3 The importance of a direct calculation of IRF and the dependence of $A_{T_{Strat}}$ on radiative kernel choice

Figure 1a (purple bars) shows the resulting NorESM2-MM ERF, IRF and adjustments. For comparison, corresponding data from the NorESM2-MM 4xCO_2 ERF experiment of Smith et al. (2020a) is also shown (green bars). As expected, the magnitude of ERF is near-equal in each experiment, at 8.40 W m^{-2} (purple bar) and 8.38 W m^{-2} (green bar). The difference of 0.02 W m^{-2} is likely attributable to differences in the time-period used to average model output, or to the use of alternate initial conditions and computing machine architecture given that all other aspects of simulation design were implemented identically (see Section 2 and Smith et al., 2020a, Section 2).

a)

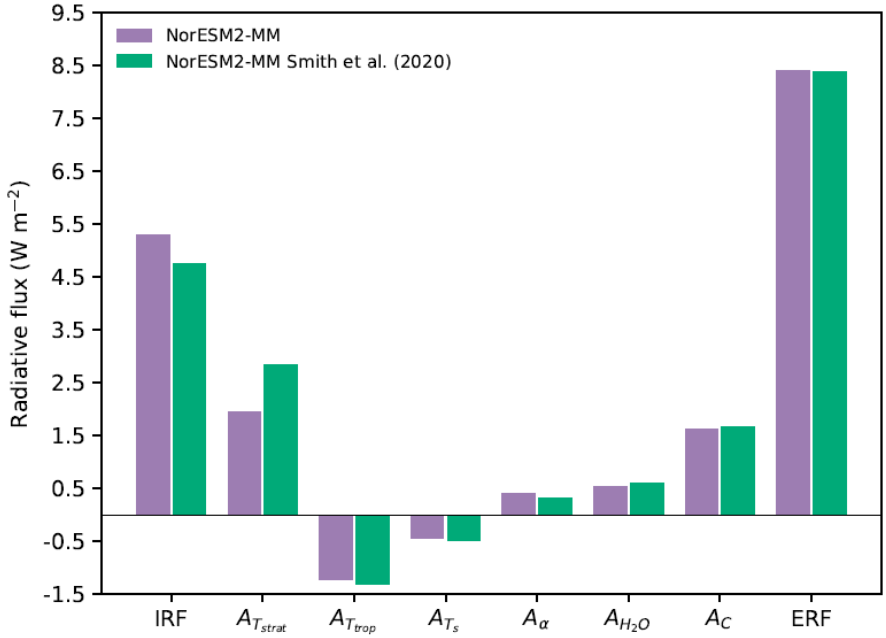

b)

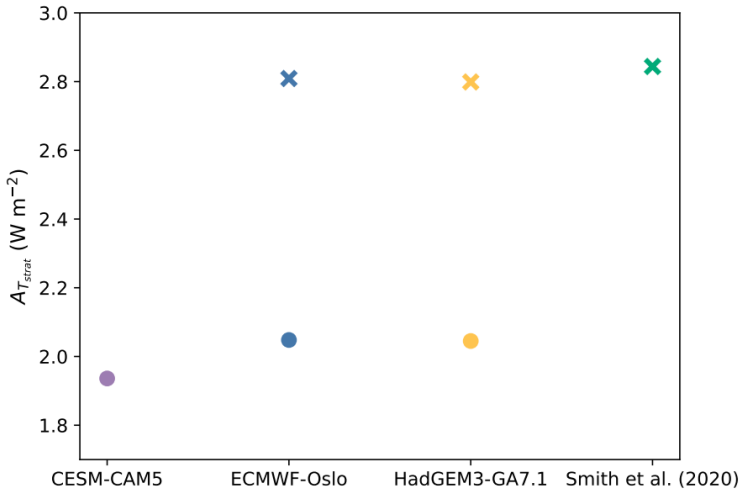

Figure 1: a) NorESM2-MM 4xCO_2 ERF and its components (purple bars) with IRF calculated using PORT and adjustments diagnosed using the CESM-CAM5 kernels. Green bars show corresponding data from Smith et al. (2020a), whereby the ERF for the same perturbation has been calculated from 30-year simulations of NorESM2-MM with adjustments calculated using the HadGEM3-GA7.1 radiative kernels and with IRF estimated as the residual of ERF minus total adjustments. b) Comparison of NorESM2-MM $A_{T_{Strat}}$ when calculated using different radiative kernels. Filled circles

represent $A_{T_{Strat}}$ calculated following the methodology outlined in Section 2, whereby NorESM2-MM output is interpolated onto the given radiative kernel pressure levels but not extrapolated to kernel pressure levels outside of the NorESM2-MM uppermost and lowermost pressures. Crosses represent the magnitude of $A_{T_{Strat}}$ if such extrapolation is performed for the ECMWF-Oslo and HadGEM3-GA7.1 kernels and the value given by Smith et al. (2020a) (which uses the HadGEM3-GA7.1 kernel).

Figure 1a further shows that the magnitude of IRF varies notably, demonstrating a dependence on the diagnostic method of choice. When calculated directly using PORT, the IRF is 0.54 W m^{-2} larger than when estimated as the difference between ERF and the sum of adjustments (as in Smith et al. 2020a), comparing 5.30 W m^{-2} (purple bar) and 4.76 W m^{-2} (green bar). This demonstrates the necessity of using a model's own radiative transfer code to calculate IRF and highlights the possibility for error in studies that derive this forcing as a residual. Directly calculating the IRF also permits the calculation of ϵ (see Eq.1) to analyse the magnitude of non-linearities that are not accounted for by the kernel-derived adjustments. Our ϵ value (calculated as ERF-IRF-ΣA_x) is 3% (0.27 W m^{-2}) of the ERF (8.40 W m^{-2}) and therefore well within the 10% guideline given by Shell et al., (2008). However, when spectrally split, the shortwave ϵ is 33% (-0.47 W m^{-2}) of the shortwave ERF (1.42 W m^{-2}) and works to partially counteract a longwave ϵ of 0.74 W m^{-2} (which itself is 11% of the longwave ERF of 6.98 W m^{-2}). This finding also extends to our analysis of the clear-sky 4xCO_2 forcing and adjustments (not shown). Such larger residuals can possibly be explained by the collapse of linear behaviour for a large perturbation like 4xCO_2 (see Jonko et al., 2012, Smith et al., 2020b). We further note the close agreement in A_c, which occurs despite the use of different methods to calculate it. In Smith et al. (2020a) shortwave and longwave A_c are estimated separately using the APRP approach and offline monthly-mean partial radiative perturbation calculations, respectively. In our approach, A_c is calculated using the adjusted CRE method (see Section 2).

The stratospheric temperature adjustment is strong and positive as anticipated due to the process of stratospheric cooling following an increase in CO_2 concentration (e.g. Myhre et al., 2013; Smith et al., 2018; Forster et al., 2021). However, there is a clear difference when comparing the value reported here (1.94 W m^{-2}, purple bar) against Smith et al. (2020a; 2.84 W m^{-2}, green bar). Because $A_{T_{Trop}}$ is similar between both experiments (-1.23 W m^{-2} vs -1.32 W m^{-2}) it can be deduced that the difference in magnitude of $A_{T_{Strat}}$ is not predominantly driven by the choice of tropopause definition (in Smith et al. (2020a) this is based on the World Meteorological Organization definition of a lapse-rate tropopause, whereby geopotential height is used as an approximation of geometric height on model pressure levels in the control integration). Instead, the difference in $A_{T_{Strat}}$ stems from the use of different radiative kernels (i.e., CESM-CAM5 vs HadGEM3-GA7.1) and the method of applying model output in the $A_{T_{Strat}}$calculation. For our derivation of $A_{T_{Strat}}$ we interpolate NorESM2-MM output to the 30 CESM-CAM5 kernel pressure levels, where 3.64 hPa is the highest level. Even though this is a 'low-top' kernel, this matches the

highest level of NorESM2-MM output meaning that the use of this kernel in the $A_{T_{Strat}}$ calculation captures all of the stratospheric cooling occurring in NorESM2-MM following a 4xCO_2 perturbation. Alternatively, Smith et al. (2020a) use the HadGEM3-GA7.1 radiative kernel, which itself has been interpolated from a native vertical resolution of 85 pressure levels (up to around 0.005 hPa) to the standard 19 CMIP6 pressure levels, with an upper bound of 1 hPa. Smith et al. (2020a) derive $A_{T_{Strat}}$ by using model output that has been interpolated and extrapolated to the 19 CMIP6 pressure levels. This therefore extends stratospheric temperatures in NorESM2-MM above the model's highest level of 3.64 hPa to 1 hPa. Whilst this method better accounts for outgoing radiation emitted to space from the upper stratosphere for each unit change in temperature, it does not represent the actual adjustment modelled by NorESM2-MM.

Figure 1b (filled circles) further demonstrates this issue by comparing the magnitude of $A_{T_{Strat}}$ calculated by applying our NorESM2-MM output to two additional kernels: ECMWF-Oslo and HadGEM3-GA7.1. The ECMWF-Oslo kernel has 60 pressure levels, with a high resolution in the stratosphere extending to 0.1 hPa, and as described above, the HadGEM3-GA7.1 utilises the standard CMIP6 19 pressure levels. When we interpolate (but do not extrapolate) NorESM2-MM output onto these pressure levels, the use of both ECMWF-Oslo and HadGEM3-GA7.1 results in an adjustment similar to that given by CESM-CAM5, at 2.05 W m^{-2} (blue and yellow filled circles). However, when NorESM2-MM output is both interpolated and extrapolated to the upper stratospheric levels of the ECMWF-Oslo and HadGEM3-GA7.1 kernels, the adjustment is notably stronger (and in closer agreement with Smith et al. 2020a) at around 2.80 W m^{-2} (blue and yellow crosses). The importance of the vertical resolution of stratosphere has been stated previously in studies quantifying the magnitude of $A_{T_{Strat}}$ to a CO_2 forcing. Notably, Smith et al. (2018) demonstrate that disagreement in 2xCO_2 $A_{T_{Strat}}$ is dependent on whether a given kernel has high stratospheric resolution (e.g., ECMWF-Oslo) and if the model output is also highly resolved in the stratosphere. Smith et al. (2020b) further report that kernels based on a high-top atmospheric model with a large number of native pressure levels have a pronounced increase in the magnitude and rate of emitted radiation at 5 hPa and 1 hPa. Here, the difference between the 'extrapolated' (blue and yellow crosses) and 'not-extrapolated' $A_{T_{Strat}}$ values (blue and yellow circles) in Fig. 1b infers that around 0.75 W m^{-2} of 'additional' stratospheric temperature adjustment occurs between the model top and the upper pressure limit of the ECMWF-Oslo and HadGEM3-GA7.1 kernels (0.1 hPa and 1 hPa, respectively). This therefore supports previous studies that highlight the significance of vertical stratospheric resolution on $A_{T_{Strat}}$ and further demonstrates that the choice and method of applying a radiative kernel can substantially impact results. Opting to use a radiative kernel that has been constructed from the same atmospheric model as the CO_2 forcing simulations in question will more accurately represent the magnitude of $A_{T_{Strat}}$ simulated within that given model. This also ensures that the calculation of $A_{T_{Strat}}$ is based entirely on one underlying radiative transfer code, which eliminates any uncertainty in the magnitude of $A_{T_{Strat}}$ that could occur if the kernel and model output were derived from two different parameterisations. If a radiative kernel is not available for a given model, or a kernel needs to be applied across multiple models to evaluate inter-model spread, then it could be more suitable to

not extrapolate data outside of each model's native vertical bounds. However, the best use of kernels is likely quite case specific.

4 Stratospheric O_3 experiments

4.1 Impact of O_3 perturbations on stratospheric temperature

O_3 plays an important role in driving the thermal structure of the stratosphere due to strong absorption of ultraviolet radiation and absorption and emission of thermal-infrared (TIR) radiation. Figure 2 (left) shows the effect of a 50% increase in stratospheric O_3 concentration on zonal-mean atmospheric temperature in the control integration of NorESM2-MM. A strong increase in stratospheric temperature is evident, consistent with enhanced absorption of solar radiation and hence enhanced solar heating rates. The peak increase in temperature occurs in the lower stratosphere centered across the equatorial region, co-located with high insolation. Here the maximum ΔT reaches 5.8 K. Similarly, decreasing stratospheric O_3 concentration by 50% results in reduced absorption of solar radiation, reduced solar heating rates and a strong cooling of the stratosphere (Fig. 2, right). As above, the peak temperature decrease occurs in the lower stratosphere across the equator, with a maximum ΔT of -9 K. The impact of reduced stratospheric O_3 also propagates into the troposphere (primarily between 70°-90°N/S), due to more downward solar irradiance reaching the lower levels of the atmosphere where enhanced absorption and heating can take place. Considering the high correlation between $4xCO_2$ IRF and 10 hPa air temperature reported by He et al. (2023), we note that at this level in particular ΔT largely increases by $\geq$ 3 K in the 'Strat O_3x1.5' case (Fig 2., left) and largely decreases by $\geq$ 4 K in the 'Strat O_3x0.5' case (Fig 2., right).

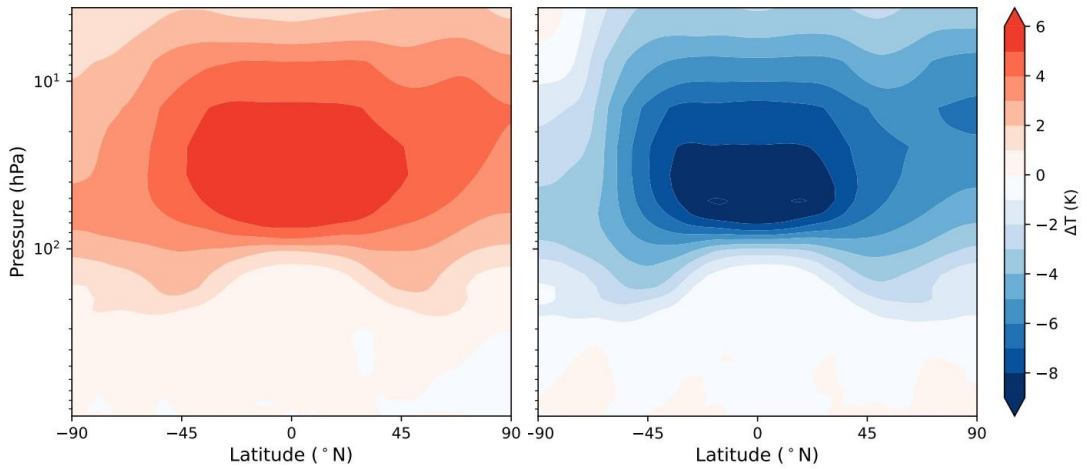

Figure 2: Zonal-mean difference in atmospheric temperature between the control integration of 'Strat O_3x1.5' and the control integration of the 'standard' 4xCO_2 ERF simulation (left) and between the control integration of 'Strat O_3x0.5' and the control integration of the 'standard' 4xCO_2 ERF simulation (right).

4.2 Impact of stratospheric O_3 perturbations on 4xCO_2 ERF and components

Figure 3 compares ERF, IRF and the individual adjustments for the 'standard' 4xCO_2, 'Strat O_3x1.5' and 'Strat O_3x0.5' experiments. As shown, increasing stratospheric O_3 by 50% has negligible impact on the magnitude of 4xCO_2 ERF in NorESM2-MM, resulting in a near identical forcing (of 8.48 W m^{-2}) compared to the 'standard' case (dark-orange bar). Similarly, the effect of decreasing stratospheric O_3 by 50% has a marginal effect on 4xCO_2 ERF, increasing the forcing by just 0.22 W m^{-2} relative to the 'standard' case. Evidently, the impact of increased/decreased O_3 concentration on stratospheric temperature (Fig. 2) does not result in a marked effect on ERF. In all three cases NorESM2-MM simulates a considerably larger ERF than the 17 CMIP6 multi-model mean of 7.98 W m^{-2} reported by Smith et al. (2020a).

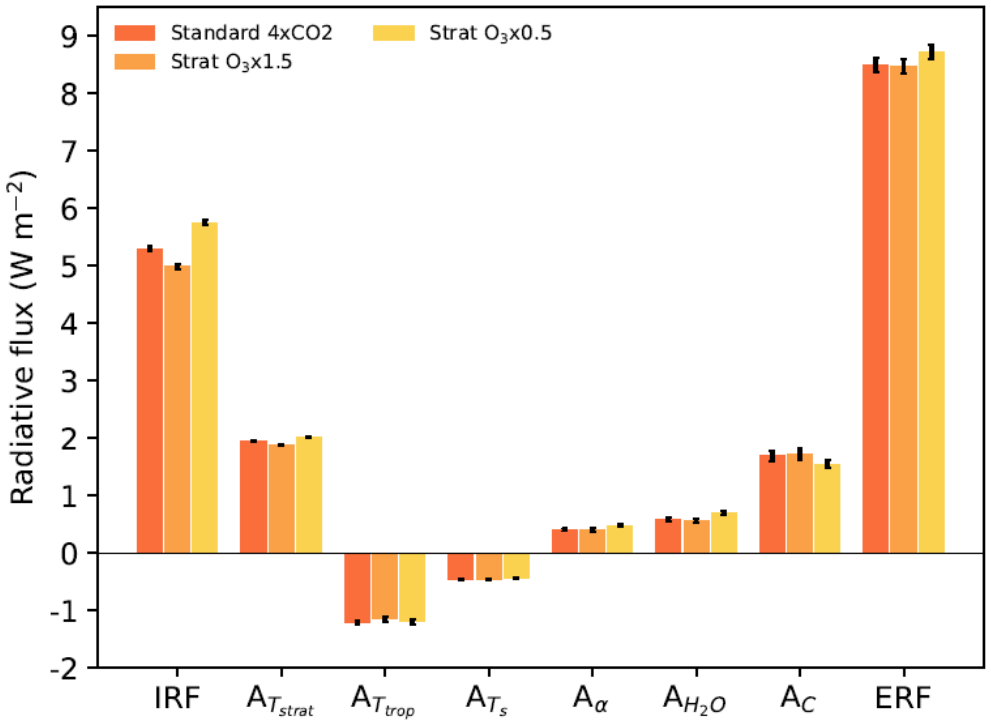

Figure 3: Comparison of NorESM2-MM 'standard' 4xCO_2 ERF, IRF and adjustments against ERF, IRF and adjustments diagnosed from the 'Strat O_3x1.5'and 'Strat O_3x0.5' experiments. All adjustments are derived using the CESM-CAM5 kernels and all components are derived from the average of years 6-15 of NorESM2-MM output, hence the values for the 'standard' 4xCO_2 case shown here differ slightly to those shown in Fig. 1. Error bars show the standard error of the mean of each component.

Analysis of $A_{T_{Strat}}$ further demonstrates that these experiments do not cause a significant effect on the magnitude of temperature adjustment throughout the stratosphere, producing just a 3% decrease and 4% increase in this component for the 'Strat O_3x1.5' and 'Strat O_3x0.5' cases, respectively. This corroborates experiments from He et al., (2023; Figure S6) that compare the size of stratospheric temperature adjustment after a quadrupling of CO_2 from two different base-states; the multi-model ensemble-mean difference in their adjustment is just -0.03 W m^{-2} (although the model range is considerably larger at around 0.5 W m^{-2}). The largest impact occurs on the IRF which increases by 8% and decreases by 6% when stratospheric O_3 is reduced and enhanced relative to the 'standard' experiment. The IRF across all three experiments ranges from 4.98 – 5.74 W m^{-2} resulting in a spread of around 0.8 W m^{-2}. This is smaller than the spread of 2 W m^{-2} (ranging from around 5 – 7 W m^{-2}) reported by He et al. (2023) for offline 'double-call' experiments of 4xCO_2 IRF calculated with a single radiative transfer code and base-states from the Atmospheric Model Intercomparison Project (AMIP) for 12 CMIP5/6 models (hence their spread

is due only to differences in base-state). However, we find closer agreement between our IRF sensitivity to 10 hPa base-state temperature and He et al. (2023), who found a near -0.1 W m^{-2} K^{-1} relation between the spread in offline double-call experiments and air temperature at this level (Figure 1c in He et al., 2023). From Figure 2 it can be inferred that this matches very well with the ~7 K difference in base-state 10 hPa temperature between 'StratO_3x1.5' and 'StratO_3x0.5' and the corresponding 0.8 W m^{-2} spread in IRF.

The effect on IRF can be explained principally by the impact of O_3 increases/decreases on base-state stratospheric temperature and secondarily by the spectral overlap of CO_2 and O_3[1]. In the 'Strat O_3x0.5' case for example, the reduced O_3 concentration induces cooling of the stratosphere, which reduces the emission of outgoing TIR irradiance at the TOA and makes the radiative impact of a 4xCO_2 perturbation more potent. The reverse is true in the 'Strat O_3x1.5' case. In relation to spectral overlap, O_3 itself possesses two fundamental absorption bands in the TIR around 9.6 μm and 14.27 μm, with a relatively strong band formed by overtone and combination transitions centered at 4.75 μm. As stratospheric O_3 concentrations increase, TIR absorption at these wavelengths also increases to an extent that depends on the level of band saturation and the abundance of other gases absorbing at these wavelengths. The opposite occurs if stratospheric O_3 concentrations decrease. For CO_2, the main TIR bands lie in the window regions of the H_2O spectrum, with absorption centered at 4.3 μm and 15 μm (the latter of which is highly significant due to its proximity to the peak of blackbody distribution for the Earth's effective emitting temperature). Weaker bands also occur near 10 μm. Regions of spectral overlap between O_3 and CO_2 therefore arise at several wavelengths; at 15 μm the strength of CO_2 absorption largely masks the radiative effect of O_3 at 14.27 μm and absorption by both gases at 4.75 μm and 4.3 μm has little impact given their location further away from the peak of Earth's blackbody distribution. However, decreased stratospheric O_3 concentration leads to weakened absorption at 9.6 μm that can enhance absorption by CO_2 at 10 μm. Likewise, increasing stratospheric O_3 concentration results in strengthened 9.6 μm absorption that mutes CO_2. Combining the effect of base-state stratospheric temperature and spectral overlap, a 4xCO_2 perturbation therefore results in an enhancement of the IRF in the 'Strat O_3x0.5' case relative to the 'standard' experiment. Correspondingly, an increase in stratospheric O_3 has the opposite (albeit evidently weaker) effect.

In discussion of the potential climate implications of their findings, He et al. (2023) suggest that O_3 depletion since the 1970s could have led to a strengthening of TOA CO_2 IRF due to the cooling of the lower stratosphere associated with O_3 loss. They theorise that the combined effect of O_3 depletion and CO_2 increase should produce a larger CO_2 ERF and a greater surface warming than model experiments that impose these perturbations separately. They calculate the indirect surface warming effect of O_3 loss by differencing surface temperature anomalies between two such sets of experiments (historical forcing between 1985-2014 vs the sum of all historical forcings between 1985-2014 imposed independently) and infer that the sign and spatial

[1]Tests performed by the GENLN2 line-by-line (Myhre et al., 2006) show that a decrease in temperature of 2 K across the whole stratosphere leads to a 0.16 W m^{-2} increase in 4xCO_2 IRF, whilst a 50% reduction in stratospheric O_3 leads to a 0.07 W m^{-2} increase in 4xCO_2 IRF.

distribution of the nonlinear warming contribution of O_3 loss to CO_2 IRF is consistent with the base-state dependence of IRF. As shown above, we demonstrate that a highly idealised reduction in stratospheric O_3 does lead to an enhancement of 4xCO_2 IRF. However, we find that this does not significantly affect the magnitude of ERF, largely because the magnitude of $A_{T_{Strat}}$ remains the same size.

5 Conclusions

Here we demonstrate that accurate calculation of IRF requires the use of host-model radiative transfer calculations, which can be computed either offline or online using double-call simulations. As noted elsewhere (e.g., Chung and Soden 2015b), we encourage modelling centres to make this diagnostic available with their simulations. Inferring IRF indirectly as the residual of ERF and the sum of adjustments can result in the erroneous estimation of its magnitude which introduces further uncertainty into the exact nature of inter-model spread in CO_2 ERF. We also show that increasing and decreasing stratospheric O_3 by 50% results in a strong warming and cooling of stratosphere, with the peak change in temperature in each experiment reaching around 6 K and -9 K, respectively. Despite the sizeable effect on stratospheric temperature, these highly idealised changes in O_3 concentration do not result in a correspondingly large spread in the magnitude of stratospheric temperature adjustment or 4xCO_2 ERF. Instead, these experiments demonstrate a dominant impact on the magnitude of IRF, chiefly due to the impact on base-state stratospheric temperature and the spectral overlap of CO_2 and O_3, whereby for example, decreasing stratospheric O_3 weakens absorption by O_3 at 9.6 μm and enhances CO_2 absorption at 10 μm, resulting in a strengthening of the greenhouse effect of CO_2 following a quadrupling of its concentration. Given that such large changes in stratospheric O_3 do not yield a significant impact on 4xCO_2 ERF, our results suggests that inter-model differences in stratospheric O_3 concentration are not predominantly responsible for inter-model spread in CO_2 forcing.

Code availability. NorESM2 (tag release-noresm2.0.6) can be downloaded from https://github.com/NorESMhub/NorESM (Seland et al., 2020).

Data availability: The CESM-CAM5 radiative kernels are freely available at https://zenodo.org/records/997902 (Pendergrass et al., 2018). The ECMWF-Oslo kernels are freely available at https://github.com/ciceroOslo/Radiative-kernels.git (Myhre et al., 2018). The HadGEM3-GA7.1 kernels are freely available at https://doi.org/10.5281/zenodo.3594673 (Smith et al., 2020b).

Author contributions. GM and REB designed the study. REB performed the simulations, with supporting calculations performed by GM and ØH. REB and GM analysed the data. REB produced the figures and was the primary writer of the manuscript with contributions from GM, DO, ØH and MS.

Competing interests. At least one of the (co-)authors is a member of the editorial board of Atmospheric Chemistry and Physics.

Acknowledgements. We thank Christopher J. Smith for his input on technical aspects of this manuscript and for his review and comments. We also thank Marit Sandstad for her technical advice on model simulations. REB and GM were supported by the European Union's Horizon 2020 research and innovation programme under grant agreement No 820829 (CONSTRAIN).

References

Andrews, T., Gregory, J. M., and Webb, M. J.: The Dependence of Radiative Forcing and Feedback on Evolving Patterns of Surface Temperature Change in Climate Models, Journal of Climate, 28, 1630-1648, https://doi.org/10.1175/JCLI-D-14-00545.1, 2015.

Andrews, T., Smith, C. J., Myhre, G., Forster, P. M., Chadwick, R., and Ackerley, D.: Effective Radiative Forcing in a GCM With Fixed Surface Temperatures, Journal of Geophysical Research: Atmospheres, 126, e2020JD033880, https://doi.org/10.1029/2020JD033880, 2021.

Boucher, O., D. Randall, P. Artaxo, C. Bretherton, G. Feingold, P. Forster, V.-M. Kerminen, Y. Kondo, H. Liao, U. Lohmann, P. Rasch, S.K. Satheesh, S. Sherwood, B. Stevens, and X.Y. Zhang: Clouds and aerosols. In Climate Change 2013: The Physical Science Basis. Contribution of Working Group I to the Fifth Assessment Report of the Intergovernmental Panel on Climate Change. , 571-657, 10.1017/CBO9781107415324.016, 2013.

Checa-Garcia, R: CMIP6 Ozone forcing dataset: supporting information, Zenodo, https://doi.org/10.5281/zenodo.1135127, 2018.

Chung, E.-S. and Soden, B. J.: An Assessment of Direct Radiative Forcing, Radiative Adjustments, and Radiative Feedbacks in Coupled Ocean–Atmosphere Models, Journal of Climate, 28, 4152-4170, https://doi.org/10.1175/JCLI-D-14-00436.1, 2015a.

Chung, E.-S. and Soden, B. J.: An assessment of methods for computing radiative forcing in climate models, Environmental Research Letters, 10, 074004, 10.1088/1748-9326/10/7/074004, 2015b.

Collins, W. D., Ramaswamy, V., Schwarzkopf, M. D., Sun, Y., Portmann, R. W., Fu, Q., Casanova, S. E. B., Dufresne, J.-L., Fillmore, D. W., Forster, P. M. D., Galin, V. Y., Gohar, L. K., Ingram, W. J., Kratz, D. P., Lefebvre, M.-P., Li, J., Marquet, P., Oinas, V., Tsushima, Y., Uchiyama, T., and Zhong, W. Y.: Radiative forcing by well-mixed greenhouse gases: Estimates from climate models in the Intergovernmental Panel on Climate Change (IPCC) Fourth Assessment Report (AR4), Journal of Geophysical Research: Atmospheres, 111, https://doi.org/10.1029/2005JD006713, 2006.

Conley, A. J., Lamarque, J. F., Vitt, F., Collins, W. D., and Kiehl, J.: PORT, a CESM tool for the diagnosis of radiative forcing, Geosci. Model Dev., 6, 469-476, 10.5194/gmd-6-469-2013, 2013.

Danabasoglu, G., Lamarque, J.-F., Bacmeister, J., Bailey, D. A., DuVivier, A. K., Edwards, J., Emmons, L. K., Fasullo, J., Garcia, R., Gettelman, A., Hannay, C., Holland, M. M., Large, W. G., Lauritzen, P. H., Lawrence, D. M., Lenaerts, J. T. M., Lindsay, K., Lipscomb, W. H., Mills, M. J., Neale, R., Oleson, K. W., Otto-Bliesner, B., Phillips, A. S., Sacks, W., Tilmes, S., van Kampenhout, L., Vertenstein, M., Bertini, A., Dennis, J., Deser, C., Fischer, C., Fox-Kemper, B., Kay, J. E., Kinnison, D., Kushner, P. J., Larson, V. E., Long, M. C., Mickelson, S., Moore, J. K., Nienhouse, E., Polvani, L., Rasch, P. J., and Strand, W. G.: The Community Earth System Model Version 2 (CESM2),

Journal of Advances in Modeling Earth Systems, 12, e2019MS001916, https://doi.org/10.1029/2019MS001916, 2020.

Etminan, M., Myhre, G., Highwood, E. J., and Shine, K. P.: Radiative forcing of carbon dioxide, methane, and nitrous oxide: A significant revision of the methane radiative forcing, Geophysical Research Letters, 43, 12,614-612,623, https://doi.org/10.1002/2016GL071930, 2016.

Eyring, V., Bony, S., Meehl, G. A., Senior, C. A., Stevens, B., Stouffer, R. J., and Taylor, K. E.: Overview of the Coupled Model Intercomparison Project Phase 6 (CMIP6) experimental design and organization, Geosci. Model Dev., 9, 1937-1958, 10.5194/gmd-9-1937-2016, 2016.

Forster, P., T. Storelvmo, K. Armour, W. Collins, J.-L. Dufresne, D. Frame, D.J. Lunt, T. Mauritsen, M.D. Palmer, M. Watanabe, M. Wild, and H. Zhang: The Earth's Energy Budget, Climate Feedbacks and Climate Sensitivity, in: In Climate Change 2021: The Physical Science Basis. Contribution of Working Group I to the Sixth Assessment Report of the Intergovernmental Panel on Climate Change, edited by: Masson-Delmotte, V., P. Zhai, A. Pirani, S.L. Connors, C. Péan, S. Berger, N. Caud, Y. Chen, L. Goldfarb, M.I. Gomis, M. Huang, K. Leitzell, E. Lonnoy, J.B.R. Matthews, T.K. Maycock, T. Waterfield, O. Yelekçi, R. Yu, and B. Zhou, Cambridge University Press, Cambridge, United Kingdom and New York, NY, USA, 923-1054, 10.1017/9781009157896.009., 2021.

Forster, P. M., Richardson, T., Maycock, A. C., Smith, C. J., Samset, B. H., Myhre, G., Andrews, T., Pincus, R., and Schulz, M.: Recommendations for diagnosing effective radiative forcing from climate models for CMIP6, Journal of Geophysical Research: Atmospheres, 121, 12,460-412,475, https://doi.org/10.1002/2016JD025320, 2016.

Gettelman, A., Mills, M. J., Kinnison, D. E., Garcia, R. R., Smith, A. K., Marsh, D. R., Tilmes, S., Vitt, F., Bardeen, C. G., McInerny, J., Liu, H.-L., Solomon, S. C., Polvani, L. M., Emmons, L. K., Lamarque, J.-F., Richter, J. H., Glanville, A. S., Bacmeister, J. T., Phillips, A. S., Neale, R. B., Simpson, I. R., DuVivier, A. K., Hodzic, A., and Randel, W. J.: The Whole Atmosphere Community Climate Model Version 6 (WACCM6), Journal of Geophysical Research: Atmospheres, 124, 12380-12403, https://doi.org/10.1029/2019JD030943, 2019.

Gregory, J. M., Ingram, W. J., Palmer, M. A., Jones, G. S., Stott, P. A., Thorpe, R. B., Lowe, J. A., Johns, T. C., and Williams, K. D.: A new method for diagnosing radiative forcing and climate sensitivity, Geophysical Research Letters, 31, https://doi.org/10.1029/2003GL018747, 2004.

Hansen, J., Fung, I., Lacis, A., Rind, D., Lebedeff, S., Ruedy, R., Russell, G., and Stone, P.: Global climate changes as forecast by Goddard Institute for Space Studies three-dimensional model, Journal of Geophysical Research: Atmospheres, 93, 9341-9364, https://doi.org/10.1029/JD093iD08p09341, 1988.

Hansen, J., Sato, M., Ruedy, R., Nazarenko, L., Lacis, A., Schmidt, G. A., Russell, G., Aleinov, I., Bauer, M., Bauer, S., Bell, N., Cairns, B., Canuto, V., Chandler, M., Cheng, Y., Del Genio, A., Faluvegi, G., Fleming, E., Friend, A., Hall, T., Jackman, C., Kelley, M., Kiang, N., Koch, D., Lean, J., Lerner, J., Lo, K., Menon, S., Miller, R., Minnis, P., Novakov, T., Oinas, V., Perlwitz, J., Perlwitz, J., Rind, D., Romanou, A., Shindell, D., Stone, P., Sun, S., Tausnev, N., Thresher, D., Wielicki, B., Wong, T., Yao, M., and Zhang, S.: Efficacy of climate forcings, Journal of Geophysical Research: Atmospheres, 110, https://doi.org/10.1029/2005JD005776, 2005.

He, H., Kramer, R. J., Soden, B. J., and Jeevanjee, N.: State dependence of CO2 forcing and its implications for climate sensitivity, Science, 382, 1051-1056, doi:10.1126/science.abq6872, 2023.

Iacono, M. J., Delamere, J. S., Mlawer, E. J., Shephard, M. W., Clough, S. A., and Collins, W. D.: Radiative forcing by long-lived greenhouse gases: Calculations with the AER radiative transfer models, Journal of Geophysical Research: Atmospheres, 113, https://doi.org/10.1029/2008JD009944, 2008.

Jeevanjee, N., Seeley, J. T., Paynter, D., and Fueglistaler, S.: An Analytical Model for Spatially Varying Clear-Sky CO2 Forcing, Journal of Climate, 34, 9463-9480, https://doi.org/10.1175/JCLI-D-19-0756.1, 2021.

Jonko, A. K., K. M. Shell, B. M. Sanderson, and G. Danabasoglu: Climate Feedbacks in CCSM3 under Changing CO2 Forcing. Part I: Adapting the Linear Radiative Kernel Technique to Feedback Calculations for a Broad Range of Forcings. *J. Climate*, **25**, 5260–5272, https://doi.org/10.1175/JCLI-D-11-00524.1, 2012

Kamae, Y. and Watanabe, M.: On the robustness of tropospheric adjustment in CMIP5 models, Geophysical Research Letters, 39, https://doi.org/10.1029/2012GL054275, 2012.

Keeble, J., Hassler, B., Banerjee, A., Checa-Garcia, R., Chiodo, G., Davis, S., Eyring, V., Griffiths, P. T., Morgenstern, O., Nowack, P., Zeng, G., Zhang, J., Bodeker, G., Burrows, S., Cameron-Smith, P., Cugnet, D., Danek, C., Deushi, M., Horowitz, L. W., Kubin, A., Li, L., Lohmann, G., Michou, M., Mills, M. J., Nabat, P., Olivié, D., Park, S., Seland,

Ø., Stoll, J., Wieners, K.-H., and Wu, T.: Evaluating stratospheric ozone and water vapour changes in CMIP6 models from 1850 to 2100, Atmos. Chem. Phys., 21, 5015–5061, https://doi.org/10.5194/acp-21-5015-2021, 2021.

Marvel, K., Schmidt, G. A., Miller, R. L., and Nazarenko, L. S.: Implications for climate sensitivity from the response to individual forcings, Nature Climate Change, 6, 386-389, 10.1038/nclimate2888, 2016.

Meinshausen, M., Nicholls, Z. R. J., Lewis, J., Gidden, M. J., Vogel, E., Freund, M., Beyerle, U., Gessner, C., Nauels, A., Bauer, N., Canadell, J. G., Daniel, J. S., John, A., Krummel, P. B., Luderer, G., Meinshausen, N., Montzka, S. A., Rayner, P. J., Reimann, S., Smith, S. J., van den Berg, M., Velders, G. J. M., Vollmer, M. K., and Wang, R. H. J.: The shared socio-economic pathway (SSP) greenhouse gas concentrations and their extensions to 2500, Geosci. Model Dev., 13, 3571-3605, 10.5194/gmd-13-3571-2020, 2020.

Myhre, G., Highwood, E. J., Shine, K. P., and Stordal, F.: New estimates of radiative forcing due to well mixed greenhouse gases, Geophysical Research Letters, 25, 2715-2718, https://doi.org/10.1029/98GL01908, 1998.

Myhre, G., F. Stordal, I. Gausemel, C. J. Nielsen, and E. Mahieu: Line-by-line calculations of thermal infrared radiation representative for global condition: CFC-12 as an example, *J. Quant. Spectrosc. Radiat. Transfer*, **97**, 317–331, doi:10.1016/j.jqsrt.2005.04.015, 2006

Myhre, G., Kramer, R. J., Smith, C. J., Hodnebrog, Ø., Forster, P., Soden, B. J., Samset, B. H., Stjern, C. W., Andrews, T., Boucher, O., Faluvegi, G., Fläschner, D., Kasoar, M., Kirkevåg, A., Lamarque, J.-F., Olivié, D., Richardson, T., Shindell, D., Stier, P., Takemura, T., Voulgarakis, A., and Watson-Parris, D.: Quantifying the Importance of Rapid Adjustments for Global Precipitation Changes, Geophysical Research Letters, 45, 11,399-311,405, https://doi.org/10.1029/2018GL079474, 2018.

Myhre, G., Shindell, D., Bréon, F. M., Collins, W., Fuglestvedt, J., Huang, J., et al. : Anthropogenic and natural radiative forcing, in: Climate change 2013: The physical science basis. Contribution of Working Group I to the Fifth Assessment Report of the Intergovernmental Panel on Climate Change, edited by: T. F. Stocker, D. Q., G. K. Plattner, M. Tignor, S. K. Allen, J. Boschung, et al. , Cambridge University Press, Cambridge, UK and New York 659–740, 2013.

Pendergrass, A. G., Conley, A., and Vitt, F. M.: Surface and top-of-atmosphere radiative feedback kernels for CESM-CAM5, Earth Syst. Sci. Data, 10, 317-324, 10.5194/essd-10-317-2018, 2018.

Pincus, R., Buehler, S. A., Brath, M., Crevoisier, C., Jamil, O., Franklin Evans, K., Manners, J., Menzel, R. L., Mlawer, E. J., Paynter, D., Pernak, R. L., and Tellier, Y.: Benchmark Calculations of Radiative Forcing by Greenhouse Gases, Journal of Geophysical Research: Atmospheres, 125, e2020JD033483, https://doi.org/10.1029/2020JD033483, 2020.

Pincus, R., Forster, P. M., and Stevens, B.: The Radiative Forcing Model Intercomparison Project (RFMIP): experimental protocol for CMIP6, Geosci. Model Dev., 9, 3447-3460, 10.5194/gmd-9-3447-2016, 2016.

Pincus, R., Mlawer, E. J., Oreopoulos, L., Ackerman, A. S., Baek, S., Brath, M., Buehler, S. A., Cady-Pereira, K. E., Cole, J. N. S., Dufresne, J.-L., Kelley, M., Li, J., Manners, J., Paynter, D. J., Roehrig, R., Sekiguchi, M., and Schwarzkopf, D. M.: Radiative flux and forcing parameterization error in aerosol-free clear skies, Geophysical Research Letters, 42, 5485-5492, https://doi.org/10.1002/2015GL064291, 2015.

Ramaswamy, V., Collins, W., Haywood, J., Lean, J., Mahowald, N., Myhre, G., Naik, V., Shine, K. P., Soden, B., Stenchikov, G., and Storelvmo, T.: Radiative Forcing of Climate: The Historical Evolution of the Radiative Forcing Concept, the Forcing Agents and their Quantification, and Applications, Meteorological Monographs, 59, 10.1175/AMSMONOGRAPHS-D-19-0001.1, 2019.

Richardson, T. B., Forster, P. M., Smith, C. J., Maycock, A. C., Wood, T., Andrews, T., Boucher, O., Faluvegi, G., Fläschner, D., Hodnebrog, Ø., Kasoar, M., Kirkevåg, A., Lamarque, J.-F., Mülmenstädt, J., Myhre, G., Olivié, D., Portmann, R. W., Samset, B. H., Shawki, D., Shindell, D., Stier, P., Takemura, T., Voulgarakis, A., and Watson-Parris, D.: Efficacy of Climate Forcings in PDRMIP Models, Journal of Geophysical Research: Atmospheres, 124, 12824-12844, https://doi.org/10.1029/2019JD030581, 2019.

Seland, Ø., Bentsen, M., Olivié, D., Toniazzo, T., Gjermundsen, A., Graff, L. S., Debernard, J. B., Gupta, A. K., He, Y. C., Kirkevåg, A., Schwinger, J., Tjiputra, J., Aas, K. S., Bethke, I., Fan, Y., Griesfeller, J., Grini, A., Guo, C., Ilicak, M., Karset, I. H. H., Landgren, O., Liakka, J., Moseid, K. O., Nummelin, A., Spensberger, C., Tang, H., Zhang, Z., Heinze, C., Iversen, T., and Schulz, M.: Overview of the Norwegian Earth System Model (NorESM2) and key climate response of CMIP6 DECK, historical, and scenario simulations, Geosci. Model Dev., 13, 6165-6200, 10.5194/gmd-13-6165-2020, 2020.

Shell, K. M., Kiehl, J. T., and Shields, C. A.: Using the Radiative Kernel Technique to Calculate Climate Feedbacks in NCAR's Community Atmospheric Model, Journal of Climate, 21, 2269-2282, https://doi.org/10.1175/2007JCLI2044.1, 2008.

Sherwood, S. C., Bony, S., Boucher, O., Bretherton, C., Forster, P. M., Gregory, J. M., and Stevens, B.: Adjustments in the Forcing-Feedback Framework for Understanding Climate Change, Bulletin of the American Meteorological Society, 96, 217-228, https://doi.org/10.1175/BAMS-D-13-00167.1, 2015.

Smith, C. J., Kramer, R. J., Myhre, G., Alterskjær, K., Collins, W., Sima, A., Boucher, O., Dufresne, J. L., Nabat, P., Michou, M., Yukimoto, S., Cole, J., Paynter, D., Shiogama, H., O'Connor, F. M., Robertson, E., Wiltshire, A., Andrews, T., Hannay, C., Miller, R., Nazarenko, L., Kirkevåg, A., Olivié, D., Fiedler, S., Lewinschal, A., Mackallah, C., Dix, M., Pincus, R., and Forster, P. M.: Effective radiative forcing and adjustments in CMIP6 models, Atmos. Chem. Phys., 20, 9591-9618, 10.5194/acp-20-9591-2020, 2020a.

Smith, C. J., Kramer, R. J., Myhre, G., Forster, P. M., Soden, B. J., Andrews, T., Boucher, O., Faluvegi, G., Fläschner, D., Hodnebrog, Ø., Kasoar, M., Kharin, V., Kirkevåg, A., Lamarque, J.-F., Mülmenstädt, J., Olivié, D., Richardson, T., Samset, B. H., Shindell, D., Stier, P., Takemura, T., Voulgarakis, A., and Watson-Parris, D.: Understanding Rapid Adjustments to Diverse Forcing Agents, Geophysical Research Letters, 45, 12,023-012,031, https://doi.org/10.1029/2018GL079826, 2018.

Smith, C. J., Kramer, R. J., and Sima, A.: The HadGEM3-GA7.1 radiative kernel: the importance of a well-resolved stratosphere, Earth Syst. Sci. Data, 12, 2157-2168, 10.5194/essd-12-2157-2020, 2020b.

Soden, B. J., Collins, W. D., and Feldman, D. R.: Reducing uncertainties in climate models, Science, 361, 326-327, doi:10.1126/science.aau1864, 2018.

Soden, B. J., Held, I. M., Colman, R., Shell, K. M., Kiehl, J. T., and Shields, C. A.: Quantifying Climate Feedbacks Using Radiative Kernels, Journal of Climate, 21, 3504-3520, https://doi.org/10.1175/2007JCLI2110.1, 2008.

Zelinka, M. D., Andrews, T., Forster, P. M., and Taylor, K. E.: Quantifying components of aerosol-cloud-radiation interactions in climate models, Journal of Geophysical Research: Atmospheres, 119, 7599-7615, https://doi.org/10.1002/2014JD021710, 2014.

Zhang, M. and Huang, Y.: Radiative Forcing of Quadrupling CO2, Journal of Climate, 27, 2496-2508, https://doi.org/10.1175/JCLI-D-13-00535.1, 2014.